Electron behaviour around the onset of magnetic reconnection

Susanne F. Spinnangr[1], Michael Hesse[2], Paul Tenfjord[1], Cecilia Norgren[1], Håkon M. Kolstø[1], Norah K. Kwagala[1], Therese Moretto Jørgensen[2], Tai Phan[3]

[1]University of Bergen
[2]NASA Ames Research Center
[3]Space Sciences Laboratory, UC Berkeley

Key Points:

- Electron distributions can be used to identify current sheets that are about to reconnect
- Onset signatures persist over extended spatial and temporal scales
- The particle distributions immediately preceding onset are characterized by features of non-gyrotropy and acceleration

Corresponding author: Susanne Fløe Spinnangr, susanne.spinnangr@uib.no

Abstract

We investigate the onset of magnetic reconnection, utilizing a fully kinetic Particle-In-Cell (PIC) simulation. Characteristic features of the electron phase-space distributions immediately before reconnection onset are identified. These include signatures of pressure non-gyrotropy in the velocity distributions, and lemon shaped distributions in the in-plane velocity directions. Further, we explain how these features form through particle energization by the out-of-plane electric field. Identification of these features in the distributions can aid in analysis of data where clear signatures of ongoing reconnection are not yet present.

1 Introduction

While magnetic reconnection is one of the most important energy conversion processes in our near space environment, on the Sun and in highly magnetized astrophysical plasmas, the question of what controls its onset is still not completely understood. Magnetic reconnection has been extensively modeled and observed in a large variety of plasma environments, such as planetary magnetospheres, the solar corona, astrophysical plasmas and in laboratories and fusion reactors on Earth (Yamada et al., 2010). If we want to understand how, where, and why magnetic reconnection occurs, we must understand what physical conditions are necessary for the onset of reconnection. It has been shown that magnetic reconnection needs thin current sheets to occur (e.g. Lui, 2004; Sitnov et al., 2019), but in-situ observations proves that this alone is not a sufficient criteria for reconnection onset (e.g. Paschmann et al., 2018; R. Wang et al., 2018; Phan et al., 2020).

The onset is difficult to study with spacecraft due to its explosive nature, and varied temporal and spatial scales. The majority of reconnection studies are done where and when the data shows clear signatures of already ongoing reconnection. These signatures include ion (e.g. Paschmann et al., 1979) and electron jets (Phan et al., 2007; Torbert et al., 2018), Hall magnetic and electric fields (M. Øieroset et al., 2001; Mozer et al., 2002; Wygant et al., 2005; Eastwood et al., 2010), and non-isotropic and non-gyrotropic particle distributions (e.g. Shuster et al., 2015; Burch, Torbert, et al., 2016; Chen, Hesse, Wang, Bessho, & Daughton, 2016; Z. Wang et al., 2019; Hesse et al., 2021).

Some simulation studies have aimed to understand the physics of reconnection onset. Hesse et al. (2001) show that the presence of non-gyrotropy in the electron pressure is necessary for the generation of the diffusive electric field in the location where the X-line will form. The electron non-gyrotropy generates a linear instability of the system which eventually causes the onset of reconnection. A thorough study of the effect of the ion to electron mass ratio and the strength of the driving, was presented in Liu et al. (2014). They found that the timing of the reconnection onset was strongly influenced by the mass ratio, thereby identifying the instability leading to reconnection onset as electron tearing. The importance of electron dynamics in reconnection onset was even further emphasized by Lu et al. (2020), who show both through observation and simulation that full scale magnetic reconnection initiates from electron-only reconnection (Phan et al., 2018) in the presence of a strong external driver.

In this study, we investigate the electron dynamics right before the initial formation of an X-line, in order to identify signatures that are indicative of an imminent onset of reconnection. Recognizing such signatures will aid in the classification of reconnecting and non-reconnecting current sheets, which can broaden our understanding of what conditions are necessary for reconnection onset. In the following section we describe our simulation setup. In section 3, we identify when onset occurs, then we discuss onset signatures in the electron phase space distributions in section 4, while section 5 is a summary and discussion about our results.

2 Simulation design

We simulate magnetic reconnection in the magnetotail using a fully kinetic, 2.5D Particle-In-Cell (PIC) simiulation. In our coordinate system, x is the reconnection outflow direction, y is the initial current direction, and z is the inflow direction. Our simulation starts with a tail-like equilibrium (Birn et al., 1975) with oppositely directed magnetic fields and a current sheet with no perturbation. The initial magnetic field configuration is given by

$$B_x = \alpha(x) \tanh\left(\alpha(x)\frac{z}{l}\right) \quad (1)$$

$$B_z = \alpha'(x)\left(-z\tanh\left(\alpha(x)\frac{z}{l}\right) + \frac{l}{\alpha(x)}\right) \quad (2)$$

$$\alpha(x) = \left(1+\frac{bx}{\gamma l}\right)^{-\gamma} \quad (3)$$

where $l = 2\ d_i$ is the half-width of the current sheet, $b = 0.05$, and $\gamma = 0.6$. To establish converging flow towards the current sheet, the top, bottom and left boundaries of the simulation domain are subjected to an electric field driver, given by

$$Left: \quad E_l = \Gamma(t)\left(\frac{z}{z_{max}}\right)^2 b_{xl} \quad (4)$$

$$Top: \quad E_t = \Gamma(t)|\frac{x_{max}-x}{x_{max}}|b_{xt} \quad (5)$$

$$Bottom: \quad E_b = \Gamma(t)|\frac{x_{max}-x}{x_{max}}|b_{xb} \quad (6)$$

which increases the asymptotic magnetic field strength (B_x) through Faraday's law and leads to current sheet thinning. The b_x terms are expressions for the z-average of B_x in the boundary cells, $\Gamma(t) = \tanh(0.1t)/\cosh^2(0.1t)$, and t is time. The electric field driver peaks around $t = 7$ before it falls off, such that the driving phase is over around $t = 35$, long before the system eventually reconnects. Similar driving mechanisms that mimic the loading of magnetic flux in the inflow regions by the solar wind have been employed in previous studies, successfully resulting in reconnection (e.g. Hesse et al., 2001; Pritchett, 2005, 2010; Liu et al., 2014).

Lengths are normalized to the ion inertial length, $d_i = \frac{c}{\omega_{pi}}$, where $\omega_{pi} = \sqrt{\frac{n_0 e^2}{\epsilon_0 m_i}}$ is the ion plasma frequency with n_0 being the initial current sheet density and m_i is the ion mass. Time is normalized to the inverse ion cyclotron frequency, $\Omega_i^{-1} = \frac{m_i}{eB_0}$, where B_0 is the initial asymptotic magnetic field. We employ a time step of $\omega_{pe}\delta t = 1$. Densities are normalized to n_0, and velocities are normalized to the ion Alfvén velocity, $v_A = B_0/\sqrt{\mu_0 m_i n_0}$. The boundary conditions are reflective in both the inflow and outflow directions. We use a total of 6.7×10^9 macro-particles, and the size of the simulation domain is 60 $d_i\times$20 d_i divided into a grid of 2048×1024 cells, leaving us with about 3200 particles per cell. The ions and electrons have a mass ratio of $\frac{m_i}{m_e} = 100$ and their temperature ratio is $\frac{T_e}{T_i} = 0.2$. The ratio of the ion plasma frequency to the electron cyclotron frequency is $\omega_{pe}/\Omega_e = 2$.

In Figure 1 we show an overview of the in-plane magnetic field (contour lines) and out-of-plane current J_y (color), for four different times. We see how the thick current sheet becomes thinner as the magnetic field in the asymptotic regions become stronger, and that the thinning continues after the driving phase is over, until reconnection occurs. The penultimate panel in Figure 1 shows the simulation at the time we will investigate in detail in the following analysis.

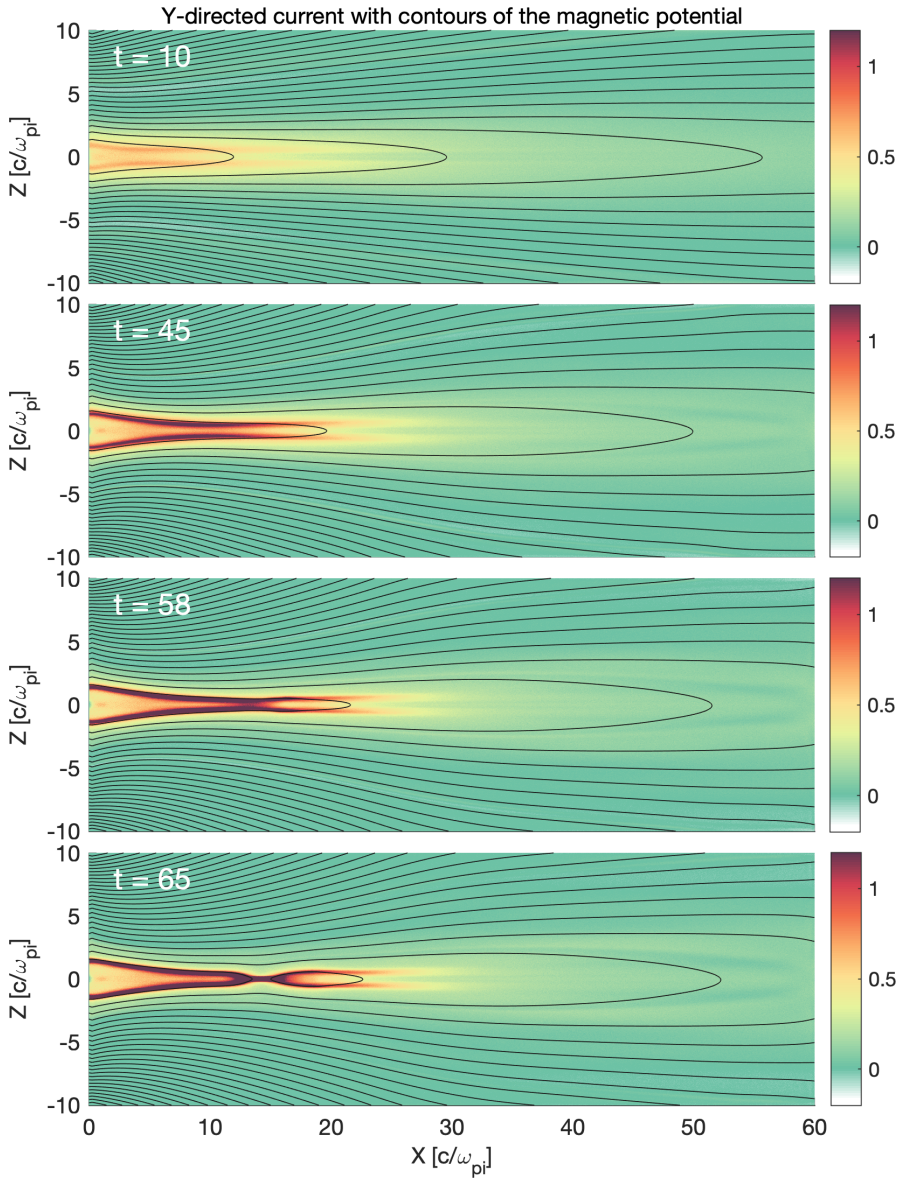

Figure 1. Evolution of the in-plane magnetic field (contours) and out-of-plane current density J_y (color). The current sheet becomes thinner and eventually reconnects. The penultimate panel shows the time of investigation, discussed later in the paper.

3 Onset of reconnection

To investigate the onset of magnetic reconnection, we must first determine when onset occurs. We follow a similar tactic as employed in (Liu et al., 2014). In our set up, the direction of B_z is initially < 0 everywhere. In order for $B_z > 0$ to appear at the neutral plane ($z = 0$), reconnection must have occurred. We therefore determine the time of investigation by finding the maximum value of $B_z(x, z = 0)$ (Figure 2a), as a function of time. An X-line forms as the max value of B_z intersects 0, which is marked in the figure with a horizontal dotted line, after which reconnection is definitely ongoing. Liu et al. (2014) determined the onset time by comparing the behaviour of B_z to a stable reference simulation in which reconnection did not occur. Onset was defined as the time when the behaviour of B_z started to deviate significantly from this reference run, in which B_z just showed a smooth change with a fairly even slope. This is similar to what we see in Figure 2a until $t \approx 55$. We have chosen to treat the last output time of our simulation before the X-line forms as the time of investigation, to ensure that we will see the system in the immediate pre-reconnection state. The time of investigation is $t = 58$, which is marked in Figure 2a with a vertical dotted line.

Next we study the off-diagonal electron pressure tensor. Magnetic reconnection can only happen in a small diffusion region where an electric field parallel to the current direction dominates the particle dynamics. This electric field is often referred to as the reconnection electric field or the diffusive electric field, and is necessary to break the frozen in condition and allow particles to diffuse across magnetic field lines. This reconnection electric field is generated through the non-gyrotropic contributions of the electron pressure tensor (Vasyliunas, 1975; Kuznetsova et al., 1998; Hesse et al., 1999, 2001). In our setup, this electric field can be expressed as

$$E_y = -\frac{1}{n_e e}\left(\frac{\partial P_{exy}}{\partial x} + \frac{\partial P_{eyz}}{\partial z}\right). \tag{7}$$

The dominating contribution around reconnection onset comes from $\partial P_{exy}/\partial x$ (Hesse et al., 2001). Figure 2b shows P_{exy} along the x-axis at $z = 0$ for the times leading up to the reconnection onset. A clear increase in P_{exy} starts to form at $t = 56$, and a significant peak is present at $x = 15$ and $t = 58$, the chosen time of investigation. The existence of this peak and consequently the gradient along x around this peak confirms that our choice of investigation time is appropriate. In the following analysis of the electron behaviour, we will investigate phase space distributions centered around this peak in P_{exy}.

4 Particle behaviour

In the preceding section we saw that a reconnection X-line forms close to $x = 15$ and $z = 0$. To investigate the electron behaviour leading up onset, we select boxes centered around this point in which we calculate the distribution functions in phase space. The boxes have $dx = 0.125\ d_i$ and $dz = 0.05\ d_i$ in each direction from their center value, such that the total length and height of each box is $0.25d_i$ and $0.1d_i$ respectively. The box sizes were chosen to optimize the resolution of the distributions without loosing statistics by having too few particles in each box. Figures 3 and 4 show maps of the reduced distribution functions $f_e(v_x, v_y)$ and $f_e(v_x, v_z)$, respectively, at $t = 58$. For completeness, a corresponding map in the $v_y v_z$ plane is included as supplementary material. In the following, we will discuss features in these distributions.

As can be seen in Figure 3, $f_e(v_x, v_y)$ is fairly similar in the different locations. This means that the features we will point out are present not only at the exact location where the X-line forms, but in a larger area around it. To aid in the analysis of the smaller scale electron behaviour, we choose to use the center distribution as an example.

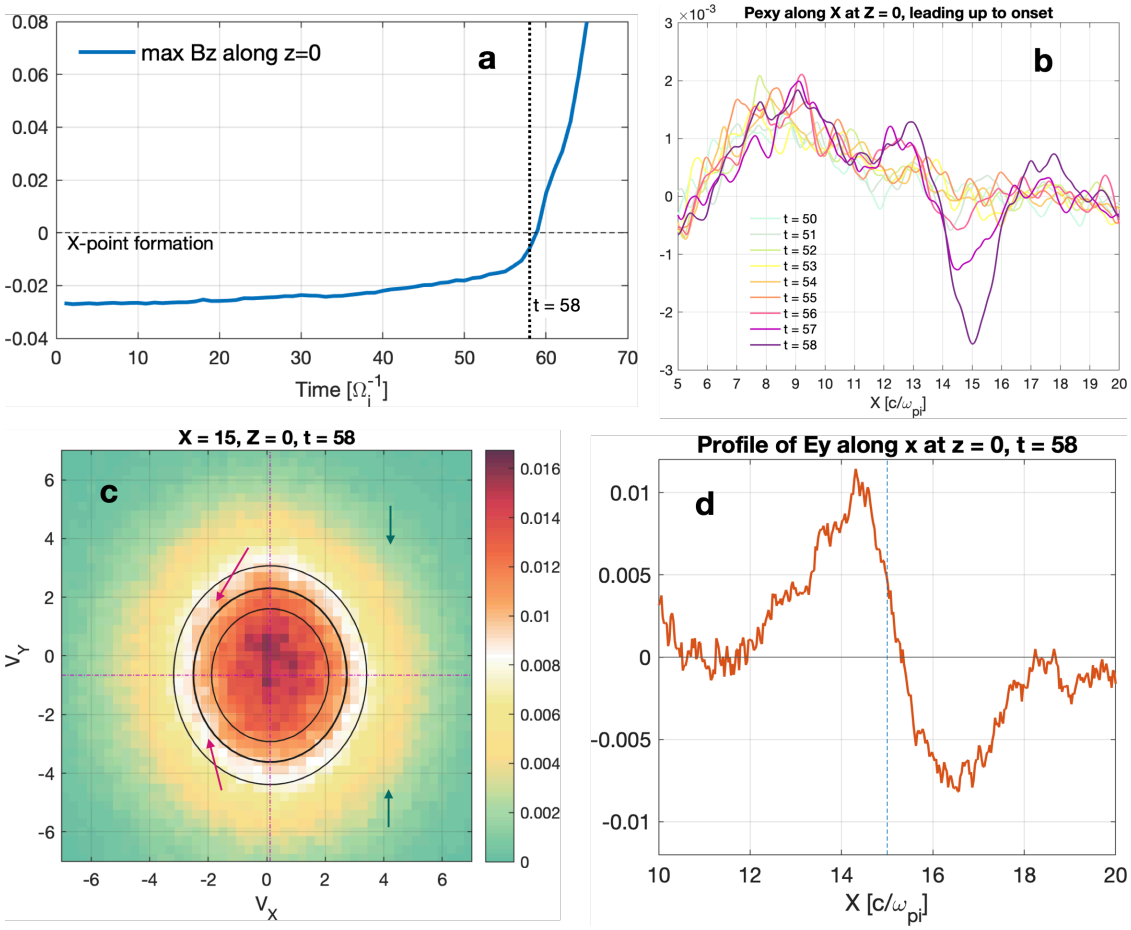

Figure 2. (a) Maximum value of B_z along $z = 0$ as a function of time. When we see a significant change in the slope of this value we are close to reconnection onset. We define the time of investigation as the last output time before the formation of the X-line (indicated by the dotted line). (b) Cut through $z = 0$ of P_{exy}, for different times leading up to the onset. The data has been averaged with a running mean in order to remove noise and extract the average behaviour. We see the necessary gradient for the generation of a diffusive electric field starts to appear and grow bigger from $t = 56$. (c) Electron distribution in the $v_x v_y$ plane, at $x = 15$, $z = 0$ and $t = 58$. The dotted pink lines show the bulk velocity. The three black contour lines show how the distribution would look if it was purely bi-Maxwellian. (d) Cut of the reconnection electric field along x at $z = 0$ and $t = 58$. The data is averaged over 0.5 d_i in the z-direction in order to reduce noise. We see that the amplitude of E_y is higher to the left of where the X-line forms than to the right. This is also true for earlier times (not shown).

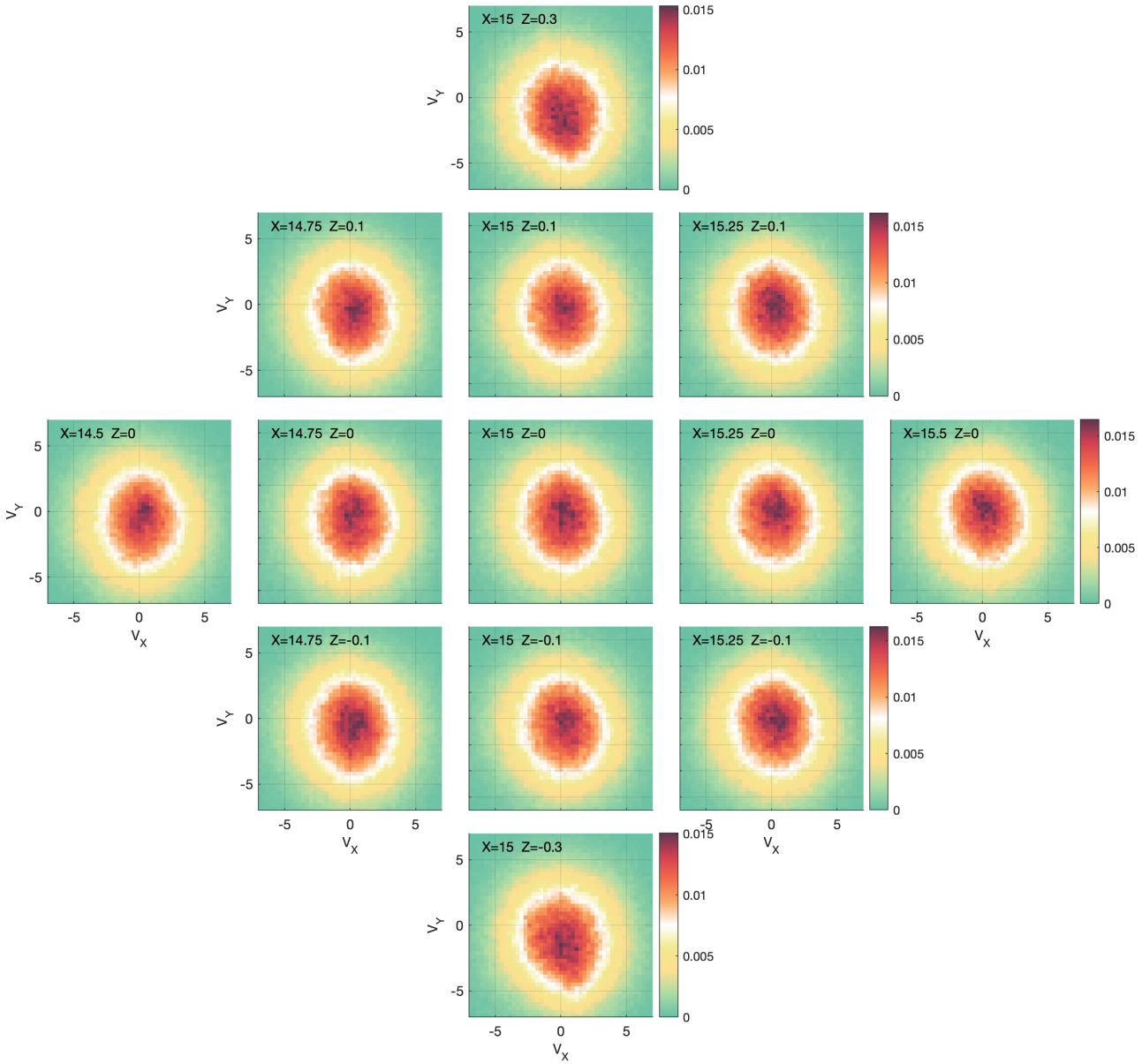

Figure 3. Reduced distributions $f_e(v_x, v_y)$ centered around the point where the contribution to the reconnection electric field from the non-gyrotropic pressure reaches a maximum at $t = 58$. The location of the center of each box is given in the top left corner of each distribution.

Figure 2c shows $f_e(v_x, v_y)$ centered around $x = 15$ and $z = 0$, at $t = 58$. The most prominent feature we see is a shift towards the negative v_y-direction. The two dotted pink lines show the bulk flow. Previously, we found that $P_{exy} \neq 0$ at this location and time. We therefore expect the distribution to show non-gyrotropic features. However, since the relative magnitude of the non-gyrotropic pressure to the total pressure is small ($P_{exy}/P_{exx} \approx 3\%$), these features are subtle. To make them easier to identify, we have overlaid the contours of a corresponding double-Maxwellian distribution, centered at the bulk flow. As it is the higher energy parts of the distribution that provides the largest contribution to the pressure, we are more interested in the features we see further away from the center than the peak around the bulk flow. For particles with negative v_x, we see a clear asymmetry between the top and bottom quadrants, indicated by the two magenta arrows. A similar, but opposite asymmetry is found for particles with positive v_x where the green arrows are pointing. If we imagine the distribution is divided vertically along the x-directed bulk flow into two semicircles, we see that the result of the asymmetries is that the two halves are shifted along the v_y-direction with respect to each other. A similar feature was found by Hesse et al. (2011) for guide field reconnection.

We can explain the shifted semicircles by taking a closer look at the history of the particles making up the distribution. In Figure 2d we show a cut of E_y at $(x, z = 0, t = 58)$. The data has been averaged over $\pm 0.5\ d_i$ in the inflow direction to reduce noise. The dotted blue line shows the x-location of the box in which we took the discussed distribution. As we can see, E_y is positive in this location, as well as to the left of it, while it turns negative to the right at $x > 15.3$. The large scale behaviour of E_y is consistent with the $\mathbf{v}\times\mathbf{B}$ drift, as the formation of a local minimum in B_z causes the frozen-in electrons to convect earthwards on the left side of $x = 15$ and tailwards on the right side. However, the reversal we see between $x = 12$ and $x = 18$ is mostly supported by the pressure divergence. The electrons are accelerated anti-parallel to E_y. This means that the electrons entering the box at $x = 15$ from the right with negative v_x are accelerated in the positive y-direction, while electrons entering from the left with positive v_x are accelerated in the negative y-direction. Additionally, the magnitude of E_y is on average slightly higher to the left of the box location than to the right. This means that particles entering this location from the left with positive v_x have on average experienced more acceleration by E_y than the particles coming from the right with negative v_x. This explains the non-gyrotropic feature of $f_e(v_x v_y)$.

This feature is visible along the $z = 0$ plane, but as can be seen in Figure 3, it is even clearer as we move out in the inflow direction. This is likely because the magnitude of E_y is greater at the boundaries where we see a larger gradient in B_x, which we will discuss below.

Figure 4 shows a map of the reduced distributions in the $v_x v_z$-plane, for the same locations as in Figure 3. As with $f_e(v_x, v_y)$, we see that the distributions display fairly similar features in all the locations. The most prominent feature is an elongation along the v_z-axis around $v_x = 0$, resulting in lemon-shaped distributions. This tells us that particles with none or very small v_x are experiencing larger acceleration in the z-direction. To explain this lemon shape, we investigate how the particles are being energized.

In Figure 5 we again choose the distribution at $x = 15$ and $z = 0$ as an example to discuss the features we see in all the distributions in Figure 4. In Figure 5a, we have chosen an example particle to trace backwards in time to investigate how it gained the accelerated v_z, indicated by the star. Figure 5 c through g show the particle position, kinetic energy, and the work done on the particle by the electric field, $-\int \mathbf{E}\cdot\mathbf{v}dt$ (including the contribution from different directions), from a time long before the onset up to the investigation time. We see that the particle has a general drift in the negative y-direction, while it is bouncing in the z-direction and mirroring in the x-direction. The amplitude of the bouncing in the z-direction is fairly constant through the full time

interval, although we do see a general change towards smaller amplitudes from about $t = 54$ and onward. Figure 5b shows cuts along z, through $x = 15$, of E_y averaged over 0.5 d_i in x, plotted as a function of time. The black contour lines are the contours of the magnetic vector potential, indicating the motion of the magnetic field at this x. The two green dotted lines indicate where $z = 0.5\ d_i$ for comparison with the particle position. We see that E_y is mostly negative and close to 0 in the center, while it is positive and with a larger amplitude further out. This is consistent with the evolution of the thinning current layer, and the generation of outer y-directed electron current layer by the $\mathbf{E}\times\mathbf{B}$-drift. The boundary between the positive and negative E_y regions is fairly stationary until around $t = 56$, from when it starts to move inwards. The short burst of positive E_y in the center just before this is a transient, temporary, large-scale fluctuation that dissipates before the time of investigation, possibly caused by reflecting waves resulting from the driving.

Comparing the position of the turning point in the z-direction with the shape of the E_y profile, we see that it coincides with the region where E_y turns positive. A closer look at the work terms in figure 5g reveals that the increase in kinetic energy comes from interactions with E_y, which results from the changing B_x. As the current sheet thins, B_x above and below it increases and propagates towards the center. This leads to a build up of E_y through Faraday's law. At the turning points in z, the particle motion is parallel to E_y, leading to energy gain through $\mathbf{E}\cdot\mathbf{v}$, as can be seen in Figure 5g. This energy gain is turned into an increased v_z as the particle continues its meandering motion. In Figure 5b, we also see the contours of the magnetic field start to move inwards and become closer together, with an increasing rate after about $t = 54$. Comparing this to the movement of the particle in z, we see the same behaviour in the amplitude of the meandering motion. This shows that the particle bounces between the magnetic walls of the inflow magnetic field. As the meandering in z and the propagation of the magnetic walls are oppositely aligned, this energy gain through E_y can also be described as simple Fermi acceleration (Fermi, 1949; Northrop, 1963). Fermi acceleration between moving regions of increased magnetic field is a common acceleration mechanism in space plasmas in general, and has recently been used to describe acceleration of electrons inside magnetic islands (Drake et al., 2006) and between merging flux ropes (Arnold et al., 2021).

5 Summary and Discussion

This study is part of a larger effort to understand why, when and where magnetic reconnection occurs. To answer these questions we must understand why some current sheets reconnect while others do not. The results of this study can be used to expand our pool of data to investigate in this regard. By being able to identify current sheets that are close to or at reconnection onset, data from current sheet observations that were previously discarded since they do not show signatures of ongoing reconnection can be included in analyses of reconnecting current sheets.

We identified two key signatures of reconnection onset in the electron distribution functions. The first is non-gyrotropy in the v_xv_y-plane, seen as shifted semicircles along the y-directed bulk flow, consistent with the necessary gradient in the non-gyrotropic electron pressure contribution to the reconnecting electric field. The second signature is lemon shaped distributions in the v_xv_z-plane due to Fermi acceleration of the electrons bouncing between the inward propagating magnetic field of the inflow regions. These distribution signatures of reconnection onset are distinct from typical distributions seen during active reconnection. Later in our simulation the electron distributions transition to exhibit the normal signatures of reconnection, such as counter-streaming electrons in the direction normal to the current sheet, cigar shapes in the inflow region and emerging crescents (not shown).

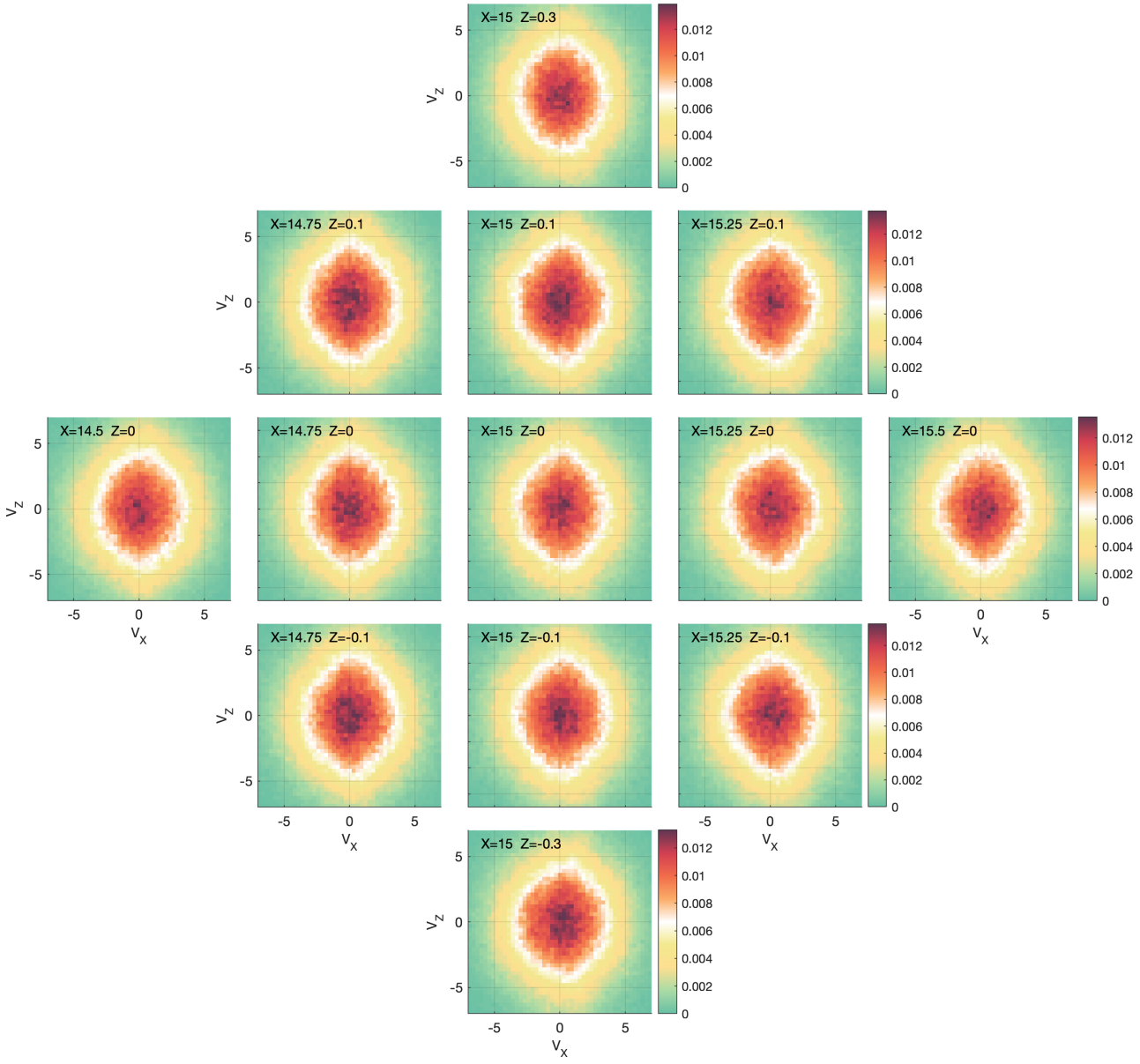

Figure 4. A map of $f_e(v_x v_z)$ for the same boxes as in Figure 3 at $t = 58$.

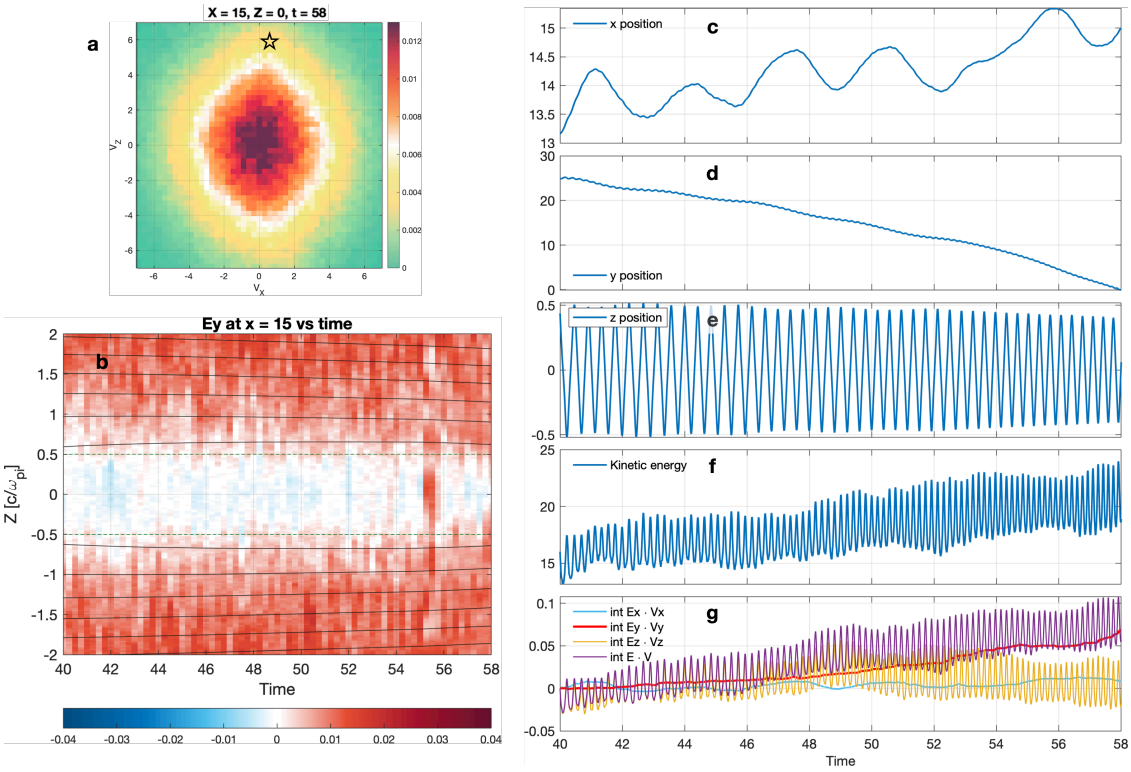

Figure 5. (a) $f_e(v_x v_z)$ at $x = 15$, $z = 0$, $t = 58$. (b) Slices along z at $x = 15$ of E_y (averaged over $0.5d_i$ in x), plotted as a function of time, with contours of the magnetic potential. (c)-(g) Position, kinetic energy and $\int \mathbf{E} \cdot \mathbf{v} dt$ for an example particle, as a function of time.

In our setup, the onset signatures are clear. The temporal resolution of the Magnetospheric Multiscale satellites (MMS) is on electron scales (Burch, Moore, et al., 2016), which is high enough that the signatures should be identifiable. If we assume $B_0 = 20\ nT$ and $n_0 \sim 0.3 - 0.8\ cm^{-3}$ (Toledo-Redondo et al., 2021), one ion cyclotron time in our simulation corresponds to about 3 s, and one ion inertial length corresponds to $255 - 420\ km$. The identified onset signatures persist over several ion times and at least a full ion inertial length around the forming X-line, which increases the probability of detection. Identifying currents sheets that show signs of being close to reconnection onset will enable us to include them in research of reconnecting currents sheets, which might further our understanding of which conditions are necessary for reconnection to occur.

Acknowledgments

This study was supported by NOTUR/NORSTOR under project NN9496K. CN and PT received support from the Research Council of Norway under contract 300865. Replication data for this study is available at (Spinnangr, 2022).

References

Arnold, H., Drake, J. F., Swisdak, M., Guo, F., Dahlin, J. T., Chen, B., ... Shen, C. (2021). Electron Acceleration during Macroscale Magnetic Reconnection. *Physical Review Letters*, *126*(13), 135101. Retrieved from `https://doi.org/10.1103/PhysRevLett.126.135101` doi: 10.1103/PhysRevLett.126.135101

Birn, J., Sommer, R., & Schindler, K. (1975). Open and closed magnetospheric tail configurations and their stability. *Astrophysics and Space Science*, *35*, 389–402.

Burch, J. L., Moore, T. E., Torbert, R. B., & Giles, B. L. (2016). *Magnetospheric Multiscale Overview and Science Objectives* (Vol. 199) (No. 1-4). doi: 10.1007/s11214-015-0164-9

Burch, J. L., Torbert, R. B., Phan, T. D., Chen, L. J., Moore, T. E., Ergun, R. E., ... Chandler, M. (2016). Electron-scale measurements of magnetic reconnection in space. *Science*, *352*(6290). doi: 10.1126/science.aaf2939

Chen, L. J., Hesse, M., Wang, S., Bessho, N., & Daughton, W. (2016). Electron energization and structure of the diffusion region during asymmetric reconnection. *Geophysical Research Letters*, *43*(6), 2405–2412. doi: 10.1002/2016GL068243

Drake, J. F., Swisdak, M., Schoeffler, K. M., Rogers, B. N., & Kobayashi, S. (2006). Formation of secondary islands during magnetic reconnection. *Geophysical Research Letters*, *33*(13), 10–13. doi: 10.1029/2006GL025957

Eastwood, J. P., Phan, T. D., Øieroset, M., & Shay, M. A. (2010). Average properties of the magnetic reconnection ion diffusion region in the Earth's magnetotail: The 2001-2005 Cluster observations and comparison with simulations. *Journal of Geophysical Research: Space Physics*, *115*(8), 1–13. doi: 10.1029/2009JA014962

Fermi, E. (1949). On the origin of the cosmic radiation. *Physical Review*, *75*(8), 1169–1174. doi: 10.1063/1.3066619

Hesse, M., Kuznetsova, M., & Birn, J. (2001). Particle-in-cell simulations of three-dimensional collisionless magnetic reconnection. *Journal of Geophysical Research: Space Physics*, *106*.

Hesse, M., Neukirch, T., Schindler, K., Kuznetsova, M., & Zenitani, S. (2011). The diffusion region in collisionless magnetic reconnection. *Space Science Reviews*, *160*(1-4), 3–23. doi: 10.1007/s11214-010-9740-1

Hesse, M., Norgren, C., Tenfjord, P., Burch, J. L., Liu, Y. H., Bessho, N., ... Kwagala, N. K. (2021). A New Look at the Electron Diffusion Region in Asymmetric Magnetic Reconnection. *Journal of Geophysical Research: Space Physics*,

126(2), 1–16. doi: 10.1029/2020JA028456

Hesse, M., Schindler, K., Birn, J., & Kuznetsova, M. (1999). The diffusion region in collisionless magnetic reconnection. *Physics of Plasmas*, *6*(5), 1781–1795. doi: 10.1063/1.873436

Kuznetsova, M. M., Hesse, M., & Winske, D. (1998). Kinetic quasi-viscous and bulk flow inertia effects in collisionless magnetotail reconnection. *Journal of Geophysical Research: Space Physics*, *103*(A1), 199–213. doi: 10.1029/97ja02699

Liu, Y. H., Birn, J., Daughton, W., Hesse, M., & Schindler, K. (2014). Onset of reconnection in the near magnetotail: PIC simulations. *Journal of Geophysical Research: Space Physics*, *119*(12), 9773–9789. doi: 10.1002/2014JA020492

Lu, S., Wang, R., Lu, Q., Angelopoulos, V., Nakamura, R., Artemyev, A. V., ... Wang, S. (2020). Magnetotail reconnection onset caused by electron kinetics with a strong external driver. *Nature Communications*, *11*(1), 1–7. doi: 10.1038/s41467-020-18787-w

Lui, A. T. Y. (2004). Potential Plasma Instabilities for Substorm Expansion Onsets. *Sp. Sci Rev.*, 127–206.

M. Øieroset, T. D. Phan, M. Fujimoto, R. P. Lin, & R. P. Lepping. (2001). In situ detection of reconnection in the Earth's magnetotail. *Nature*, *412*(July), 414.

Mozer, F. S., Bale, S. D., & Phan, T. D. (2002). Evidence of Diffusion Regions at a Subsolar Magnetopause Crossing. *Physical Review Letters*, *89*(1), 1–4. doi: 10.1103/PhysRevLett.89.015002

Northrop, T. G. (1963). Adiabatic Charged-Particle Motion. *Reviews of Geophysics*, *I*(August).

Paschmann, G., Haaland, S. E., Phan, T. D., Sonnerup, B. U., Burch, J. L., Torbert, R. B., ... Fuselier, S. A. (2018). Large-Scale Survey of the Structure of the Dayside Magnetopause by MMS. *Journal of Geophysical Research: Space Physics*, *123*(3), 2018–2033. doi: 10.1002/2017JA025121

Paschmann, G., Sonnerup, B. U., Papamastorakis, I., Sckopke, N., Haerendel, G., Bame, S. J., ... Elphic, R. C. (1979). Plasma acceleration at the Earth's magnetopause: Evidence for reconnection. *Nature*, *282*(5736), 243–246. doi: 10.1038/282243a0

Phan, T. D., Bale, S. D., Eastwood, J. P., Lavraud, B., Drake, J. F., Oieroset, M., ... Velli, M. (2020). Parker Solar Probe In Situ Observations of Magnetic Reconnection Exhausts during Encounter 1 . *The Astrophysical Journal Supplement Series*, *246*(2), 34. doi: 10.3847/1538-4365/ab55ee

Phan, T. D., Drake, J. F., Shay, M. A., Mozer, F. S., & Eastwood, J. P. (2007). Evidence for an elongated (>60 ion skin depths) electron diffusion region during fast magnetic reconnection. *Physical Review Letters*, *99*(25), 1–4. doi: 10.1103/PhysRevLett.99.255002

Phan, T. D., Eastwood, J. P., Shay, M. A., Drake, J. F., Sonnerup, B. U., Fujimoto, M., ... Magnes, W. (2018). Electron magnetic reconnection without ion coupling in Earth's turbulent magnetosheath. *Nature*, *557*(7704), 202–206. doi: 10.1038/s41586-018-0091-5

Pritchett, P. L. (2005). Externally driven magnetic reconnection in the presence of a normal magnetic field. *Journal of Geophysical Research: Space Physics*, *110*(A5). doi: 10.1029/2004JA010948

Pritchett, P. L. (2010). Onset of magnetic reconnection in the presence of a normal magnetic field: Realistic ion to electron mass ratio. *Journal of Geophysical Research: Space Physics*, *115*(10), 1–9. doi: 10.1029/2010JA015371

Shuster, J. R., Chen, L. J., Hesse, M., Argall, M. R., Daughton, W., Torbert, R. B., & Bessho, N. (2015). Spatiotemporal evolution of electron characteristics in the electron diffusion region of magnetic reconnection: Implications for acceleration and heating. *Geophysical Research Letters*, *42*(8), 2586–2593. doi: 10.1002/2015GL063601

Sitnov, M., Birn, J., Ferdousi, B., Gordeev, E., Khotyaintsev, Y., Merkin, V., ...

Zhou, X. (2019). Explosive Magnetotail Activity. *Space Science Reviews*, *215*(4). Retrieved from http://dx.doi.org/10.1007/s11214-019-0599-5 doi: 10.1007/s11214-019-0599-5

Spinnangr, S. F. (2022). *Replication data for: Electron behaviour around the onset of magnetic reconnection.* DataverseNO. Retrieved from https://doi.org/10.18710/Z2XUSW doi: 10.18710/Z2XUSW

Toledo-Redondo, S., André, M., Aunai, N., Chappell, C. R., Dargent, J., Fuselier, S. A., ... Vines, S. K. (2021). Impacts of Ionospheric Ions on Magnetic Reconnection and Earth's Magnetosphere Dynamics. *Reviews of Geophysics*, *59*(3). doi: 10.1029/2020rg000707

Torbert, R. B., Burch, J. L., Phan, T. D., Hesse, M., Argall, M. R., Shuster, J., ... Saito, Y. (2018). Electron-scale dynamics of the diffusion region during symmetric magnetic reconnection in space. *Science*, *362*(6421). doi: 10.1126/science.aat2998

Vasyliunas, V. M. (1975). Theoretical models of magnetic field line merging. *Reviews of Geophysics*, *13*(1), 303–336. doi: 10.1029/RG013i001p00303

Wang, R., Lu, Q., Nakamura, R., Baumjohann, W., Huang, C., Russell, C. T., ... Giles, B. (2018). An Electron-Scale Current Sheet Without Bursty Reconnection Signatures Observed in the Near-Earth Tail. *Geophysical Research Letters*, *45*(10), 4542–4549. doi: 10.1002/2017GL076330

Wang, Z., Fu, H. S., Liu, C. M., Liu, Y. Y., Cozzani, G., Giles, B. L., ... Burch, J. L. (2019). Electron Distribution Functions Around a Reconnection X-Line Resolved by the FOTE Method. *Geophysical Research Letters*, *46*(3), 1195–1204. doi: 10.1029/2018GL081708

Wygant, J. R., Cattell, C. A., Lysak, R., Song, Y., Dombeck, J., McFadden, J., ... Mouikis, C. (2005). Cluster observations of an intense normal component of the electric field at a thin reconnecting current sheet in the tail and its role in the shock-like acceleration of the ion fluid into the separatrix region. *Journal of Geophysical Research: Space Physics*, *110*(A9), 1–30. doi: 10.1029/2004JA010708

Yamada, M., Kulsrud, R., & Ji, H. (2010). Magnetic reconnection. *Reviews of Modern Physics*, *82*(1), 603–664. doi: 10.1103/RevModPhys.82.603